Control by atomic layer deposition over the chemical composition of nickel cobalt oxide for the oxygen evolution reaction

RESEARCH ARTICLE | APRIL 17 2023

Control by atomic layer deposition over the chemical composition of nickel cobalt oxide for the oxygen evolution reaction

Special Collection: Atomic Layer Deposition (ALD)

Renee T. M. van Limpt; Marek Lavorenti; Marcel A. Verheijen; ... et. al

Journal of Vacuum Science & Technology A 41, 032407 (2023)
https://doi.org/10.1116/6.0002414

JVST A
Journal of Vacuum Science & Technology A

ARTICLE

avs.scitation.org/journal/jva

Control by atomic layer deposition over the chemical composition of nickel cobalt oxide for the oxygen evolution reaction

Cite as: J. Vac. Sci. Technol. A 41, 032407 (2023); doi: 10.1116/6.0002414
Submitted: 9 December 2022 · Accepted: 13 March 2023 ·
Published Online: 17 April 2023

Renee T. M. van Limpt,[1,a)] Marek Lavorenti,[2] Marcel A. Verheijen,[1] Mihalis N. Tsampas,[2] and Mariadriana Creatore[2,3]

AFFILIATIONS

[1]Department of Applied Physics, Eindhoven University of Technology, 5600 MB Eindhoven, The Netherlands
[2]Dutch Institute for Fundamental Energy Research (DIFFER), De Zaale 20, 5612AJ Eindhoven, The Netherlands
[3]Eindhoven Institute of Renewable Energy Systems (EIRES), PO Box 513, 5600 MB Eindhoven, The Netherlands

Note: This paper is part of the 2024 Special Topic Collection on Atomic Layer Deposition (ALD).
[a)]**Electronic mail:** r.t.m.v.limpt@tue.nl

ABSTRACT

Anion exchange membrane water electrolysis (AEMWE) is a promising technology for renewable electricity-driven water splitting toward hydrogen production. However, application of AEMWE at industrial scale requires the development of oxygen evolution reaction (OER) electrocatalysts showing long-term stability under mild alkaline conditions. Among these, nickel cobalt oxide thin films are considered promising candidates. The ideal chemical composition of these oxides remains debatable, with recent literature indicating that rock-salt $NiCoO_2$ may exhibit similar OER activity as the traditional spinel $NiCo_2O_4$. In this work, we present the development of a plasma-enhanced atomic layer deposition (ALD) process of nickel cobalt oxide thin films (~20 nm) with focus on the role of their chemical composition and crystal structure on the OER activity. The film composition is tuned using a supercycle approach built upon CoO_x cycles with $CoCp_2$ as a precursor and O_2 plasma as a co-reactant and NiO_x cycles with $Ni(^{Me}Cp)_2$ as a precursor and O_2 plasma as a co-reactant. The films exhibit a change in the crystallographic phase from the rock-salt to spinel structure for increasing cobalt at. %. This change is accompanied by an increase in the Ni^{3+}-to-Ni^{2+} ratio. Interestingly, an increase in electrical conductivity is observed for mixed oxides, with an optimum of $(2.4 \pm 0.2) \times 10^2$ S/cm at 64 at. % Co, outperforming both NiO and Co_3O_4 by several orders of magnitude. An optimal electrocatalytic performance is observed for 80 at. % Co films. Cyclic voltammetry measurements simultaneously show a strong dependence of the OER-catalytic performance on the electrical conductivity. The present study highlights the merit of ALD in controlling the nickel cobalt oxide chemical composition and crystal structure to gain insight into its electrocatalytic performance. Moreover, these results suggest that it is important to disentangle conductivity effects from the electrocatalytic activity in future work.

I. INTRODUCTION

The massive adoption of fossil fuels causes a growing concern for environmental issues as well as global energy demand. In answer to these challenges, the growth of renewable energy- (such as wind and solar) generated electricity is accelerating world-wide.[1,2] These intermittent and fluctuating energy sources require, at the same time, the adoption of efficient, cost-effective, and robust electricity storage technologies.[3] A very promising approach is the storage of electricity surplus in hydrogen via water electrolysis. Furthermore, hydrogen is also in major demand from chemical industry and refineries. Currently, hydrogen is produced from coal, oil, or natural gas, which makes it responsible for approximately 900 Mt of direct CO_2 emissions a year.[4] Thus, it is of the utmost importance to produce low-carbon hydrogen in a cost-effective and energy-efficient manner.

Current large-scale hydrogen electrolysis production focuses on alkaline water electrolysis (AWE) and proton exchange

membrane water electrolysis (PEMWE). AWE has relatively low capital costs as no precious materials are required. The liquid electrolyte, however, limits the ability of the electrolyzer to dynamically respond to changes in hydrogen production rates and start-up/shut-down cycling, which makes the technique incompatible with the intermittent nature of renewables.[4–6] The use of a solid electrolyte in PEMWE, on the other hand, makes the technique able to quickly respond to power fluctuations. This allows to operate PEMWE with intermittent energy sources. The acidic nature of the membrane, however, results in a harsh, corrosive environment, which requires the adoption of noble metal-based electrocatalysts.[7–10] Anion exchange membrane water electrolysis (AEMWE, Fig. 1), instead, aims at combining the advantages of AWE and PEMWE by using a polymer exchange-membrane electrolysis system in an alkaline environment. The solid electrolyte makes the technique compatible with intermittent energy sources, while its alkaline environment retains the possibility to use cost-effective, earth-abundant electrocatalysts.[9,11,12]

AEMWE has only emerged this decade, and its commercialization and widespread adoption require still much effort.[13,14] The present focus of this technology is on the development of AEM materials and components. On the membrane electrode assembly level, the development of membranes and electrodes is of high importance.[8,14,15] The membranes are generally formed by a polymer backbone with anchored cationic groups that create anion selectivity. The major challenge of these materials is their limited thermal stability under basic conditions, which poses limits to both the long-term stability of AEM electrolyzers and the electrolyzer operational temperature. The development of stabilized functional groups on the polymer backbone has, fortunately, created major improvement in the chemical stability.[8,11–13,16]

The focus of this work is, therefore, on the electrocatalyst design. The oxygen evolution reaction (OER) electrocatalyst design is especially important because of the large overpotentials associated with the OER, thereby enhancing the electricity consumption and limiting the overall water splitting efficiency. The large overpotentials are due to the inherently complex four-electron transfer process ($4\ OH^- \leftrightarrow 2\ H_2O + O_2 + 4e^-$). It is kinetically favorable for OER to occur through multiple one-electron transfer reactions. At each step, enough energy must be accumulated to overcome the high kinetic energy barriers, leading to sluggish kinetics and resulting in a large overpotential.[17] The optimization of the electrocatalyst generally relies on generating a high density of active sites and intrinsic activity. To achieve a high density of catalytically active sites, it is critical to properly integrate the catalyst in the membrane electrode assembly (MEA). Traditional powder catalysts are integrated in the MEA using a binder to create a mechanically stable catalyst layer. The binder is found to often inhibit the exposure of active sites and diffusion of gas bubbles.[6,14,18,19] It is, therefore, preferred to use self-supported electrocatalysts, in which the active material is directly grown on a conductive substrate with a large surface area without the use of a binder. If no (conductive) binder is used, it is also critical that the electrocatalyst shows high electrical conductivity to drive the OER.[6,9,14]

Transition metal oxides have shown to be a promising class of OER electrocatalysts. They have remarkable catalytic activities due to their flexible oxidation states and variation in coordination structures of metal centers. Further advantages can be found in their cost-effectiveness with regard to noble metal oxides and their excellent alkali resistance.[14,20–22] Spinel cobalt oxide (Co_3O_4, Fig. 2), composed of one Co^{2+} in a tetrahedral site and two Co^{3+} ions in octahedral sites, has received significant attention as promising OER-electrocatalyst, especially due to its long-term stability at a

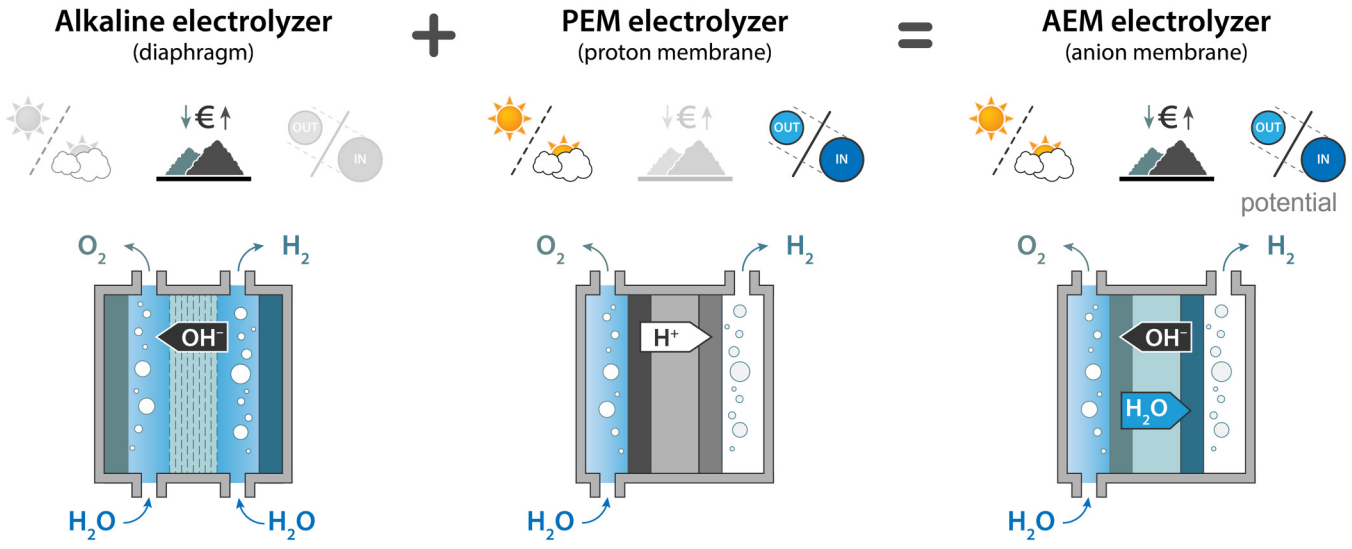

FIG. 1. Illustration visualizing the potential of the anion exchange membrane (AEM) water electrolyzer, which aims to combine the cost-effectiveness of the alkaline electrolyzer with the compatibility with intermittent energy sources and high efficiency of the proton exchange membrane (PEM) electrolyzer.

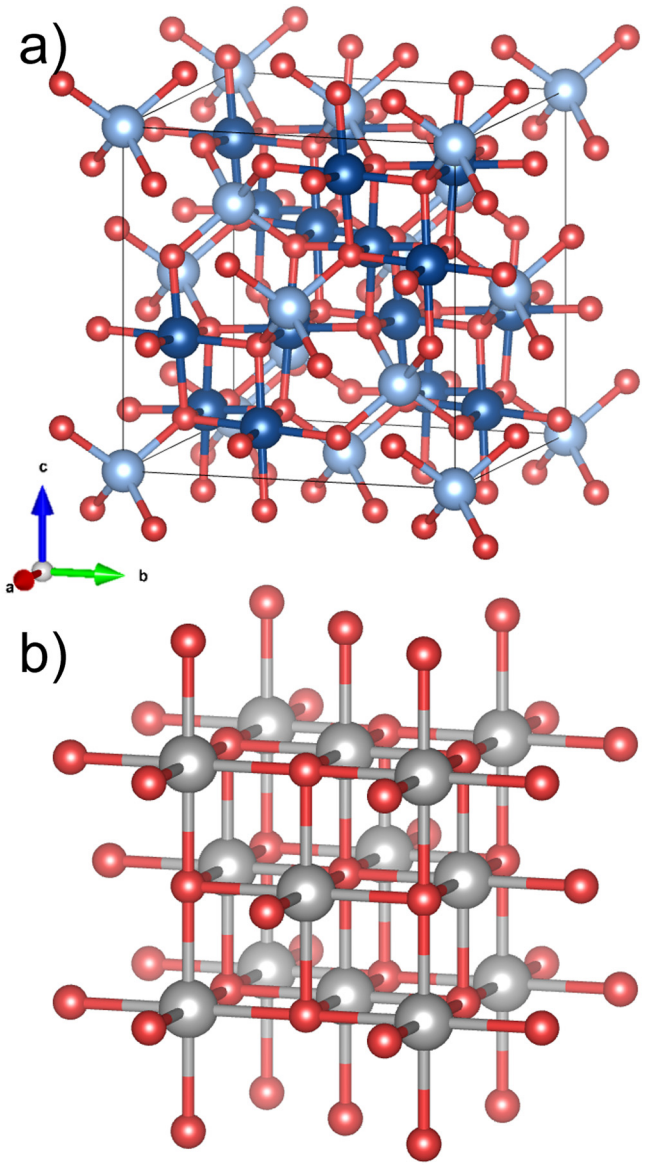

FIG. 2. Structural model of the crystallographic structure of (a) Co_3O_4 and (b) NiO. Oxygen is represented by red spheres, Co^{2+} (tetrahedral sites) by light blue spheres. Co^{3+} (octahedral sites) by dark blue spheres and nickel by gray spheres. The crystal structure is visualized using the VESTA software. (Ref. 23).

high current density.[14,24–26] Inclusion of nickel in the structure has shown to significantly improve the electrocatalytic activity.[27–30] In the spinel structure, the nickel is localized mainly on the octahedral sites to form an inverse spinel $Ni_xCo_{2-x}O_4$ structure.[31] The enhanced performance of the bimetallic oxide is mainly attributed to the incorporation of Ni^{3+}. The Fermi energy level shifts toward the valence band maximum due to Ni^{3+} hole doping, while simultaneously a new (unoccupied) hole state with Ni 3d character above the Fermi energy is formed, which enhances the hybridization of O2p states with Ni and Co 3d states. This reduces the energy barrier for electron transfer from 1.2 eV for Co_3O_4 to 0.4 eV for $NiCo_2O_4$. The unique electronic structure also reduces the energy barrier for *OH absorption, which is considered the OER rate-determining step, and facilitates the electron transfer from reaction intermediates to the catalyst.[27,32–36]

Nickel cobalt oxides can, however, also adopt the NiO rock-salt structure (Fig. 2), which contains only +2 oxidation states ($Ni_xCo_{1-x}O_2$). This phase is also shown to have good electrocatalytic performance.[34,37–41] The electrocatalytic ability of the rock-salt phase is related to its structural ability to form the highly active layered (oxy)hydroxide species.[32,38,40] Currently, there is very limited research[34,38,39,42] on the nickel cobalt oxide chemical composition, crystallographic phase, and oxidation state and their influence on the OER catalytic performance.

To investigate this effect, a technique with excellent control over film chemical composition is required. Atomic layer deposition (ALD) is a self-limiting deposition method based on cyclic and sequential dosing of gas/vapor phase species. Its self-limiting behavior originates from chemisorption reactions between the selected precursor and functional groups at the substrate surface. An ALD process consists of at least one precursor and one co-reactant that are exposed to substrates during two half-cycles. The self-limiting nature of ALD allows for digital control over film thickness and chemical composition. ALD also delivers films with high conformality, which is appealing for growth on high surface area substrates. The chemisorption of the ALD precursor with the surface functional groups also ensures that no binder material is required. ALD is, therefore, also highly suitable for the development of a self-supported electrocatalyst on high surface area electrodes. The benefit of using ALD for catalysis applications has previously been shown,[41,43–49] notably for phosphate/phosphide,[50,51] tin oxide,[43,52] or manganese oxide[53,54] catalysts for electrochemical water splitting.

In this work, we report on the influence of chemical composition and crystallographic properties of ALD-prepared nickel cobalt oxide films on its OER catalytic performance evaluated on planar substrates in a liquid three electrode system. Research on the synthesis of nickel cobalt oxides by ALD has been reported,[55,56] yet only Hagen *et al.*[56] have addressed the phase transition from a rock-salt to spinel phase. In their study, relatively thick films (~48 nm) were deposited, aiming primarily for the spinel phase and providing limited chemical characterization. To the authors' best knowledge, an extensive ALD process characterization, such as saturation curves and temperature window, has not been reported yet in literature, nor have ALD-produced nickel cobalt oxides been applied for water splitting. This study will, therefore, address the ALD process development as well as chemical, electrical, and crystallographic characterization of cobalt nickel oxides, along with their OER activity in alkaline environment as a first step before the integration of catalysts on gas diffusion electrodes.

II. EXPERIMENTAL DETAILS

A. ALD of nickel cobalt oxides

The ALD processing is carried out in a home-built plasma-enhanced ALD reactor, described elsewhere.[57] Briefly, the

system consists of a inductively coupled plasma source (13.56 MHz) and a deposition chamber. The pumping system comprises of a turbomolecular pump connected to a rotary vane pump, capable of reaching a base pressure of $<1 \times 10^{-6}$ mbar. The reactor walls are heated at 100 °C, while the substrate holder, suitable for fitting a 4 in. diameter substrate, is heated at 300 °C. Cobaltocene ($CoCp_2$, 98% purity) and 1,1′-dimethylnickelocene [$Ni(^{Me}Cp)_2$, 97% purity], both purchased from Sigma-Aldrich, are selected as precursors for the process and a 100 W O_2 plasma is selected as a reactant in the process. The $Ni(^{Me}Cp)_2$ precursor is contained in a stainless steel cylindrical bubbler heated to 55 °C and carried to the chamber through a 75 °C line using Ar gas. The $CoCp_2$ bubbler is heated to 80 °C and dosed using a Ar carrier gas through a 100 °C carrier line.

A supercycle approach based on recipes for cobalt oxide[58] and nickel oxide[59] previously developed in our group is selected for nickel cobalt oxide deposition. The process, with dosing times determined upon investigation of the self-limiting behavior and purging times,[58,59] is illustrated in Fig. 3. In short, the process consisted of 4 s of $Ni(^{Me}Cp)_2$ or $Co(Cp)_2$ precursor dosing with 4 s of Ar purging and 5 s pumping followed by, respectively, 3 or 5 s of O_2 plasma dosing and 1 s O_2 purging and 3 s pumping. One supercycle consists of x cycles of nickel oxide, followed by y cycles of cobalt oxide and is denoted as Co:Ni y:x. The ratio between the number of cycles is varied to tune the chemical composition and, therefore, also the crystal structure of the material.

B. Film characterizations

The thickness of the films is monitored during the ALD process using *in situ* spectroscopic ellipsometry (SE) with a J.A. Woollam, Inc. M2000U (1.25–3.9 eV) ellipsometer. For cobalt atomic concentrations over 75 at. % Co, the dielectric function is parameterized using a combination of a Tauc–Lorentz and two Lorentz oscillators as described by Donders *et al.*[58] Films with a cobalt content below 25 at. % Co are modeled using a combination of two Tauc–Lorentz oscillators as reported in the previous work by Lu *et al.*[60] Growth per supercycle (GPSC) is monitored based on a supercycle process consisting of five ALD cycles, respectively, Co:Ni 4:1 and Co:Ni 1:4, which is repeated 60 times. The pump time after the variable dosing time was extended to a total of 10 s (purge plus pump time) to prevent any CVD contribution. The first 48 supercycles are deposited to ensure that a closed layer is formed. The GPSC is determined using film thicknesses derived from *in situ* ellipsometry on the final 12 supercycles.

The crystal phases of the cobalt oxide and nickel oxide are investigated by grazing incidence x-ray diffraction (GI-XRD) using a Bruker Discover D8, utilizing Cu Kα (λ = 1.54060 Å) radiation in the 2θ range from 20° to 80°. Additional studies of crystal phases of nickel cobalt oxides are performed using electron diffraction with a JEOL ARM 200F Transmission Electron Microscope, operated at 200 kV, equipped with a 100 mm^2 Centurio SDD EDX detector, for the compositional homogeneity studies. Radially averaged intensity curves were extracted from electron diffraction patterns using the PASAD plug-in[61] in Gatan Digital Micrograph. All electron diffraction patterns were calibrated by Si diffraction spots originating from the transparent edge of the crystalline Si frame of the TEM window. Thus, all patterns had an internal calibration, thereby reducing the inaccuracy in the lattice parameters to <1%. X-ray photoelectron spectroscopy (XPS) is performed to investigate the chemical composition of the ALD films using a Thermo Scientific KA1066 spectrometer equipped with monochromatic Al Kα x rays. The binding axis was calibrated by using the adventitious C1s peak at 284.8 eV as a reference. Chemical composition, expressed in cobalt atomic concentration as at. % Co = 100% • (Co/ (Co + Ni)), is calculated from XPS (Fig. S1 in the supplementary material)[62] and verified by Rutherford Backscattering Spectrometry (RBS). RBS, elastic recoil detection (ERD), and particle-induced x-ray emission (PIXE) were carried out by Detect99[63] to determine the composition and mass density of the films. A 2000 keV He^+ beam is applied for both ERD and RBS. ERD was performed with a 75° sample tilt and the detector at a recoil angle of 25°. RBS is performed with perpendicular incidence and two detectors at scattering angles of 170° and 107°. Channeling mode is used to reduce the background under the oxygen peak. With RBS, it is not possible to distinguish Co from Ni. Therefore, PIXE has been used to determine the Co/Ni ratio. For PIXE, a 2.7 MeV H^+ beam at perpendicular incidence has been applied. The x-ray detector is positioned at an angle of 45° between the beam and the specimen normal, and 30 μm Kapton has been used as an absorber. The PIXE spectra have been analyzed with the Gupix[64] PIXE simulation package, and the resulting Co/Ni ratio is entered as a Co_xNi_y "molecule" in the WiNDF[65] RBS simulation package to determine the absolute amounts. A Signatone four-point probe (FPP) in combination with a Keithley 2400 Sourcemeter is employed to measure the electrical resistivity at room temperature.

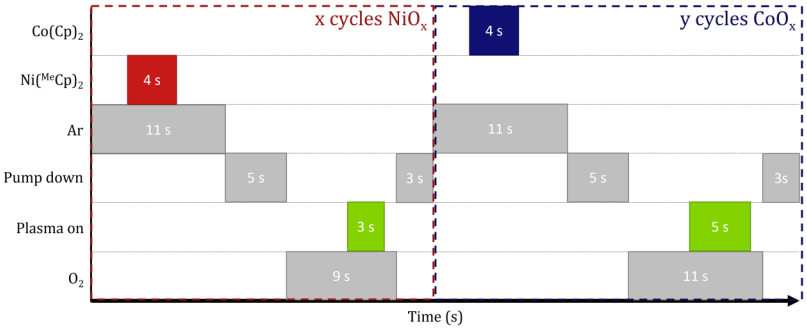

FIG. 3. Schematics of one supercycle of the ALD process used for deposition of nickel cobalt oxides.

The electrochemical performance is measured using cyclic voltammetry (CV) in a standard 150 ml electrochemical cell in three-electrode configuration equipped with a multi-channel electrochemical analyzer (Ivium-n-Stat). A graphite rod (6/70 mm, www.redox.me) is used as a counter electrode in combination with a reversible hydrogen electrode (RHE) reference electrode (mini HydroxFlex, Gaskatel). The working anode ALD films coated on FTO glass are used in a (www.redox.me) 25×25 mm sample holder with an appropriate window that allows 1 cm^2 geometric area to be exposed to the electrolyte. Measurements are executed in 1M KOH in aqueous solution (VWR chemical) at a scan rate of 10 mV s^{-1}. Electrochemical impedance spectroscopy (EIS) (Fig. S8 in the supplementary material)[62] has been used to determine the cell resistance, and 80% iR compensation has been applied to the results.

c-Si(100) with native oxygen is used as a substrate for *in situ* and *ex situ* characterization of the process. Four-point probe measurements (FPP) are conducted on highly resistive 450 nm SiO_2-coated substrates. For top-view TEM studies, depositions were performed on SiN_x TEM windows. Fluorine-doped tin oxide glass (TEC 10, $20 \times 15 \times 1.1$ mm) purchased from Ossila and cleaned by 10 min of subsequent soap water, acetone, and IPA sonication is used as a substrate for electrocatalytic performance screening. All samples are cleaned with a 15 min oxygen plasma before deposition to remove adventitious carbon from the silicon surface and establish a SiO_2-terminated surface.

III. RESULTS AND DISCUSSION

A. ALD process

Saturation curves for each dosing step of the ALD process are recorded to investigate its self-limiting behavior. The saturation curve for each dosing step of the ALD process is evaluated by independently varying the dosing times of the precursors/co-reactants. The self-limiting behavior of the $Ni(^{Me}Cp)_2$ exposure is investigated with a supercycle process consisting of one cobalt cycle and four nickel cycles (Co:Ni 1:4), while the self-limiting behavior of the $CoCp_2$ exposure cycle is examined using a process consisting of four cobalt cycles and one nickel cycle (Co:Ni 4:1). The saturation curves have been determined using *in situ* spectroscopic ellipsometry, and for different stoichiometries, different ellipsometry models need to be adopted. The Co:Ni 1:4 film has a rock-salt crystallographic structure, without traces of spinel phase. The NiO ellipsometry model consisting of two Tauc–Lorentz oscillators[60] is, therefore, employed to study the film growth rate. The Co:Ni 4:1 film, on the other hand, produces a pure spinel crystallographic phase. The growth rate is, therefore, studied using a previously developed Co_3O_4 model[58] consisting of a combination of a Tauc–Lorentz and two Lorentz oscillators.

The data reported in Fig. 4 show the self-limiting behavior of the four dosing steps. The dosing times selected for the deposition recipe are 4 s $Ni(^{Me}Cp)_2$ dosing, 3 s O_2 plasma after $Ni(^{Me}Cp)_2$ dosing and 4 s $CoCp_2$ dosing, and 5 s O_2 plasma after $CoCp_2$ dosing. The ALD temperature window is in the range 100–300 °C (Fig. S3 in the supplementary material).[62] Within this temperature window, a decrease in GPSC is observed for Co:Ni 1:4. This result agrees with the observation of Koushik *et al.*[59] for NiO, referring either to film densification or dehydroxylation at the surface. For Co:Ni 4:1, a constant GPSC is observed until 300 °C, which is a slightly lower temperature when compared to Co_3O_4 as reported by Donders *et al.*[58] This difference presumably originates from the lower temperature window of $Ni(^{Me}Cp)_2$-based NiO.[59]

The ALD process without $Ni(^{Me}Cp)_2$ dosing [Fig. 4(a)] results in the deposition of cobalt oxide with a growth per cycle (GPC) of 0.48 ± 0.02 Å, which is in agreement with the report by Donders *et al.*[58] The ALD process without $CoCp_2$ dosing [Fig. 4(c)] results in the deposition of nickel oxide with a GPC of 0.25 ± 0.03 Å, which corresponds to the report by Koushik *et al.*[59] The GPSC of Co:Ni 1:4 shows limited growth as compared to the linear combination of one CoO_x cycle and four NiO_x cycles (GPSC of 1.3 Å resp. 1.7 Å). The GPSC of Co:Ni 4:1, on the other hand, shows enhanced growth as compared to the linear combination of four CoO_x cycles and one NiO_x cycle (GPSC of 2.5 Å resp. 2.3 Å). This suggests that the presence of two transition metals affects the growth behavior of the combined ALD process, which will be discussed in future work. Consequently, the at. % Co in the material cannot be inferred by the cycle ratio in combination with the GPC of individual oxides. This study, therefore, relies on ERD, RBS, and XPS to characterize the cobalt atomic concentrations.

B. Film chemical composition and oxidation states

The chemical composition of the ALD-prepared films is verified using RBS and ERD (Table I). The films contain a negligible level of impurities in terms of hydrogen and carbon, with the carbon levels below the detection limit of 10 TFU ("thin film units", 1 TFU = 10^{15} atom/cm^2) for most films. The density of the films is determined using RBS measurements and the SE-derived thickness. The densities of Co_3O_4 and NiO are well in agreement with previous ALD deposited films[50,58,66,67] and bulk densities of 6.11 and 6.72 g/cm^3, respectively.[68] A decrease in density is observed for increasing at. % Co, which can be attributed to the incorporation of the less dense CoO phase (6.44 g/cm^3)[68,69] at low at. % Co and to the formation of the spinel phase at higher at. % Co. PIXE measurements confirm that the at. % Co can be tuned by ALD. The comparison of the RBS with XPS data, i.e., in terms of at. % Co (Fig. S1/2 in the supplementary material),[62] shows slight deviations. These are mainly attributed to (i) the overlap of the Ni KL and Co KM features in PIXE and (ii) the presence of multiple Auger features in the Ni2p and Co2p XPS spectra. As literature primarily reports XPS data, for the sake of consistency in the rest of this study, the at. % Co as determined by XPS will be mentioned.

XPS measurements (Fig. 5) of the monometallic oxide films show the oxidation states of Ni and Co expected for NiO and Co_3O_4, respectively. The exact assignment in the XPS spectra of first-row transition metals to specific chemical environments is non-trivial due to the complexity of the 2p spectra, and it is, therefore, heavily relying on assignments reported in literature[59,70–73] In the NiO spectrum, the Ni2p feature [Fig. 5(b)] at 854 eV is ascribed to the Ni^{2+} oxidation state, while the feature at 855 eV in general includes both contribution from the Ni^{3+} oxidation state and contribution from the Ni^{2+} oxidation state.[73] This means that the presence of the feature at 855 eV does not necessarily point to the the presence +3 oxidation states. The proportionality between both

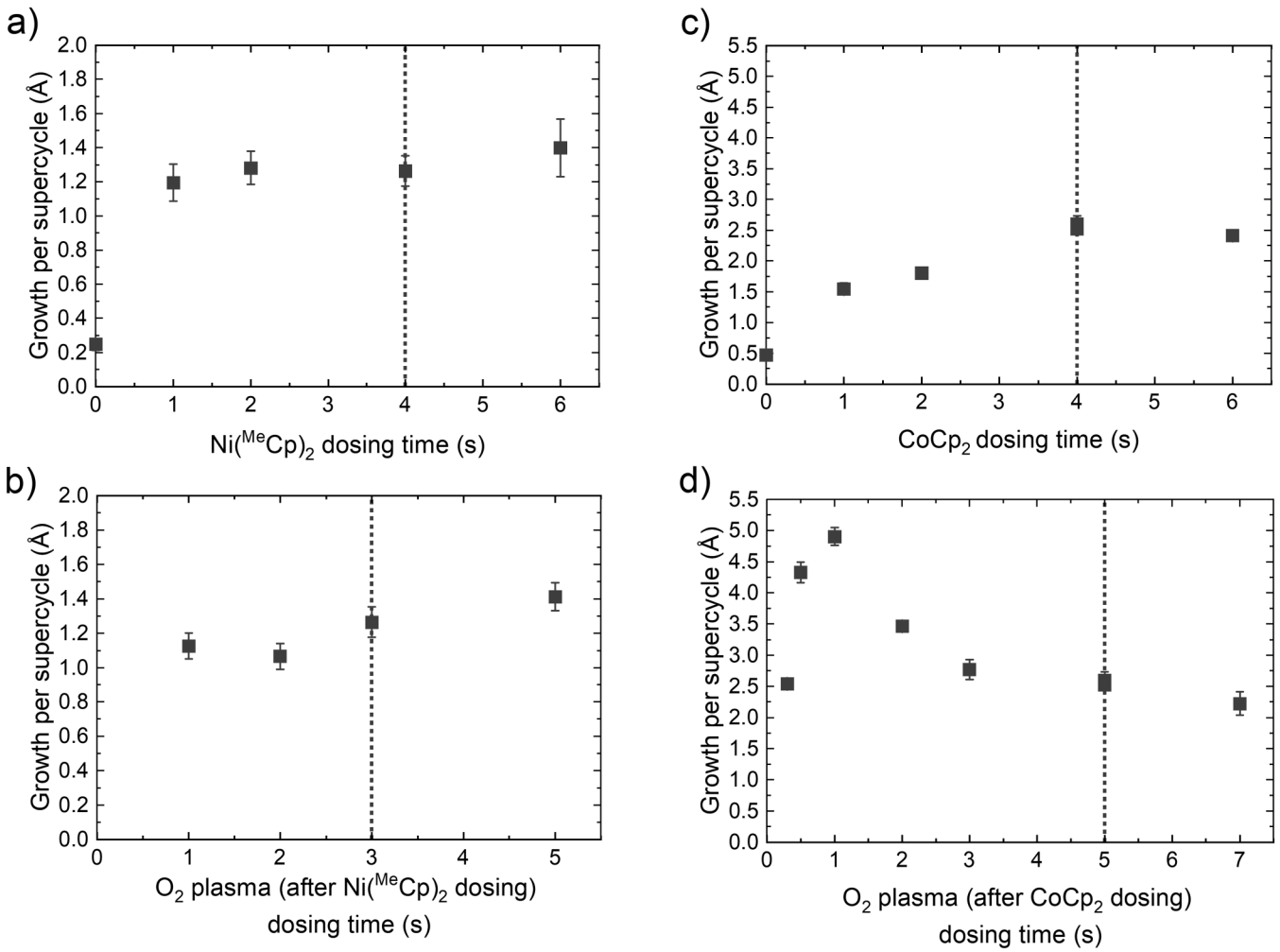

FIG. 4. Saturation curves of the four ALD steps used for deposition of cobalt nickel oxide films. (a) $Ni(^{Me}Cp)_2$ dosing and (b) O_2 plasma dosing after $Ni(^{Me}Cp)_2$ dosing are based on a Co:Ni 1:4 supercycle process and (c) $CoCp_2$ dosing and (d) O_2 plasma dosing after $CoCp_2$ dosing are based on a Co:Ni 4:1 supercycle process. The two values reported for 0 s of dosing for $Ni(^{Me}Cp)_2$ and $CoCp_2$ indicate the GPC for CoO_x and NiO_x, respectively. The selected exposure times for the standard deposition process are indicated by vertical dashed lines.

TABLE I. Elemental concentrations in nickel cobalt oxides as determined by ERD (hydrogen) and RBS. The at. % Co is determined using PIXE measurements and compared to concentrations extracted from XPS.

Sample	Thickness (nm)	H (10^{15} atoms per cm^2_{geo})	C	O	Co	Ni	Density (g/cm^3)	Co/(Co + Ni) (%) PIXE	Co/(Co + Ni) (%) XPS
Co_3O_4	9 ± 1	6 ± 1	<10	70 ± 5	39 ± 1	—	6.2 ± 0.6	—	—
NiO	17 ± 1	14 ± 1	<10	112 ± 5	—	84 ± 2	6.7 ± 0.3	—	—
Co:Ni 14:1	22 ± 2	11 ± 1	<10	153 ± 6	88 ± 2	9.6 ± 0.2	6.2 ± 0.4	90.2 ± 0.2	87 ± 1
Co:Ni 1:10	18 ± 1	13 ± 1	<10	109 ± 5	5.9 ± 0.1	82 ± 2	6.4 ± 0.2	6.7 ± 0.1	18 ± 1
Co:Ni 3:2	—	56 ± 5	25 ± 8	249 ± 7	94 ± 2	79 ± 2	—	54.5 ± 0.5	59 ± 2

features is used to determine the relative Ni^{3+}-to-Ni^{2+} ratio for different films. In the Co2p spectrum of Co_3O_4 [Fig. 5(a)], the main $2p^{3/2}$ and $2p^{1/2}$ features are observed at 795 and 780 eV, respectively, in agreement with literature.[70,72] The 15 eV energy split is indicative of the mixed Co^{2+} and Co^{3+} valence states and is characteristic of Co_3O_4 as opposed to CoO, which has the wider 16 eV feature split.[70,72] Measurements of NiO in the Co2p spectrum [Fig. 5(a)] reveal the presence of a Ni Auger feature between 780 and 770 eV, directly beneath the $Co2p^{3/2}$ feature. This hinders the observation of the cobalt oxidation states in the mixed oxides. Accurate determination of the cobalt chemical state in the mixed oxides, therefore, relies on the $2p^{1/2}$ satellite features between 800 and 810 eV, where a more intense satellite feature at slightly lower binding energy is indicative of a lower Co^{3+}-to-Co^{2+} ratio and, therefore, of the rock-salt phase.[70,72] Care is taken to subtract the Ni Auger feature from the Co2p spectrum for determination of cobalt atomic percentages (Fig. S2 in the supplementary material).[62]

XPS measurements on the 25 at. % Co film show a shift of the Ni2p spectrum (Fig. 5) to slightly higher binding energies as compared to NiO, which can be attributed to the presence of cobalt. No change in intensity of the Ni^{3+}-related shoulder as compared to the Ni^{2+} main feature is observed, which is in line with the structural analysis showing that both NiO and 25 at. % Co films are compatible to the rock-salt structure. The structural analysis based on x-ray and electron diffraction is presented in Sec. III C. The rock-salt phase obtained from the structural analysis can also be inferred by the Co2p spectrum of the 25 at. % film, which shows both a significant increase in the 800–810 eV satellite feature as compared to the Co_3O_4 spectrum as well as a 16 eV split between $2p^{3/2}$ and $2p^{1/2}$ main features, thereby confirming the presence of Co^{2+} states in a cobalt nickel alloy. An increased amount of Co^{2+} states is also observed for the 50 at. % Co film, as indicated by 15.7 eV peak splitting. This suggests, in line with the structural analysis, that there is still a significant amount of rock-salt phase present, although the presence of more Co^{3+} indicates the simultaneous presence of the spinel phase. The 75 at. % Co film, on the other hand, closely resembles the mixed Co^{2+}/Co^{3+} state of the Co_3O_4 spectrum. This suggests that a purely spinel crystallographic phase is expected to be formed.

These observations are further confirmed by the Ni2p spectrum, where a gradual increase in the amount of Ni^{3+} states is observed for the concentrations above 25 at. % Co. Given the observation of the spinel phase at 75 at. % Co during the film crystal phase analysis addressed in Sec. III C, and the corresponding characteristic mixed Co^{2+}/Co^{3+}oxidation states in the Co2p spectrum at 75 at. % Co, it can be concluded that Ni^{3+} oxidation states are also present in the spinel structure. More extensive measurements of the Ni2p spectrum show that the Ni^{3+}-to-Ni^{2+} ratio increases almost linearly between 25 at. % Co and pure Co_3O_4 (Fig. S6 in the supplementary material).[62] The formation of the Ni^{3+} oxidation state in spinel $NiCo_2O_4$ can be explained as follows: in spinel Co_3O_4, the Co^{2+} is located at the tetrahedral sites and Co^{3+} at the octahedral sites. The inverse nature of $NiCo_2O_4$, however, has Ni^{2+} ideally occupying octahedral sites and Co^{3+} occupying both octahedral and tetrahedral sites. The Co^{3+} at tetrahedral sites, however, is thermodynamically unstable, leading to the formation of the more

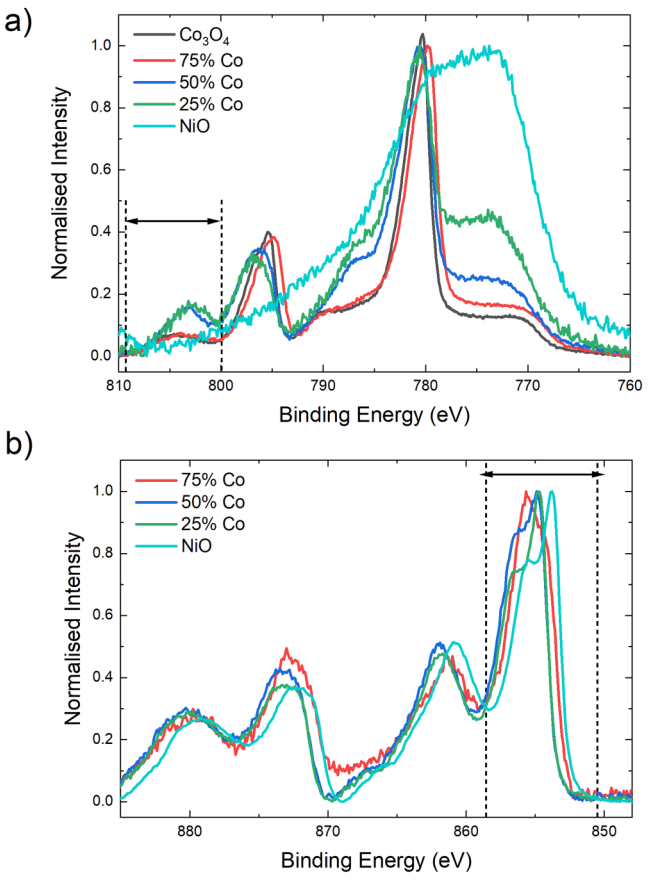

FIG. 5. XPS spectra normalized to the maximum intensity of each trace of the (a) Co2p and (b) Ni2p region of films with various at. % Co. The cobalt oxidation states are determined from splitting between the main features and $2p^{1/2}$ satellite features as indicated by dashed lines due to the presence of Ni Auger features in the Co $2p^{3/2}$ spectra. The nickel oxidation states are determined from Ni^{2+} 854 eV contribution and the Ni^{3+} 855 eV contribution indicated by dashed lines. Note that 855 eV Ni^{3+} satellite features contain contributions from the Ni^{2+} oxidation state, hampering a semiquantitative analysis on the Ni^{2+}-to-Ni^{3+} ratio.

stable Co^{2+} state. To subsequently maintain charge neutrality, a similar amount of Ni^{2+} is then converted to Ni^{3+}.[27,33,74–76]

C. Crystallographic properties

The crystallographic structures of the deposited cobalt and nickel oxides are determined by GIXRD, and the results are shown in Fig. 6. The nickel oxide diffractogram shows broad features in the region of 37°, 43°, and 63°, which are identified as (111), (200), and (220) features of the rock-salt structure, respectively.[41,59] In the cobalt oxide diffractogram, features at 31°, 37°, 59°, and 65° are identified as (220), (311), (511), and (440) features of the spinel type structure.[56] The absence of features at 42° and 61° in Fig. 6(b), the (200) and (220) rock-salt phase features,[55] indicates that the cobalt oxide is purely in the spinel crystallographic phase. In line

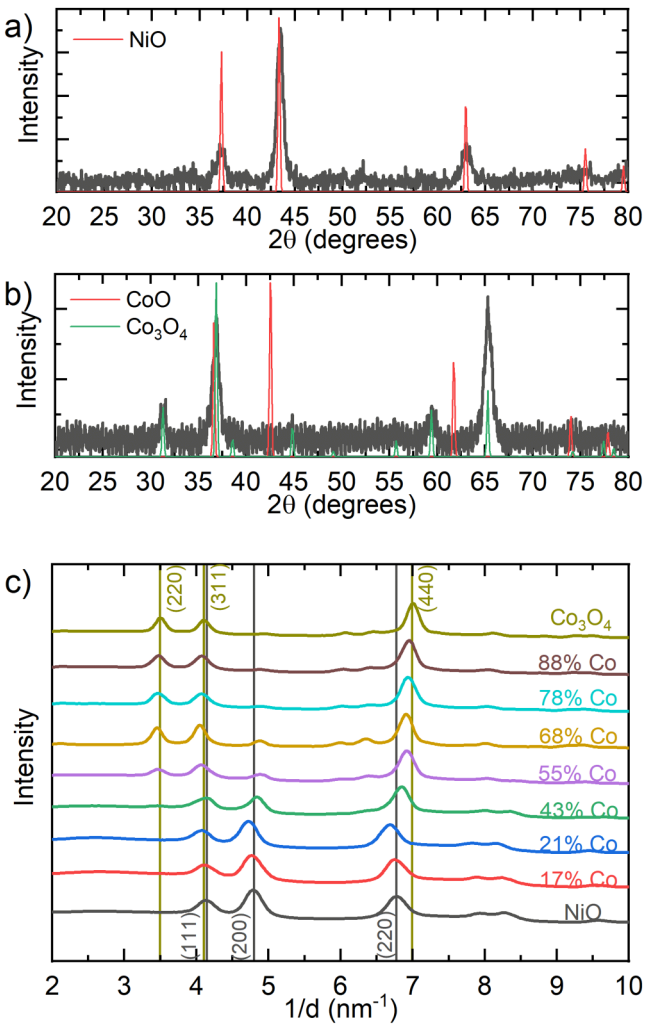

FIG. 6. GIXRD diffractogram of the ALD (a) NiO_x and (b) CoO_x film. Reference diffractograms of NiO, CoO, and Co_3O_4 are provided as obtained from ICSD database (collection codes 9866, 9865, and 36 256, respectively). (c) Radially averaged intensity curves extracted from electron diffraction patterns of ALD-deposited cobalt nickel oxide films at several at. % Co. The main features of the Co_3O_4 spinel structure and NiO rock-salt structure have been indicated with vertical lines as a guide to the eye.

with the XPS results, it can, therefore, be concluded that polycrystalline rock-salt NiO and polycrystalline spinel Co_3O_4 are formed.

Fluorescence effects between Cu Kα x rays and cobalt limit the resolution of cobalt-rich samples, and electron diffraction is, therefore, employed to study the crystallographic nature of mixed oxides [Fig. 6(c)]. Similar diffractograms from electron diffraction and GIXRD are observed for Co_3O_4 and NiO, verifying our approach. Comparison of mixed oxides with less than 25 at. % Co to the NiO diffractogram reveals only rock-salt phase features at these concentrations. The rock-salt features are observed to shift to lower 1/d, where d is the lattice spacing, for increasing at. % Co. This can be attributed to the incorporation of Co^{2+} states into the rock-salt structure, as validated by XPS.[77] The diffractograms of mixed oxides with more than 75 at. % Co only show the features characteristic of the spinel structure. The features shift to higher 1/d for increasing at. % Co as opposed to the negative shift observed for cobalt inclusion in the rock-salt structure. This shift can be explained by the inverse nature of the $NiCo_2O_4$ spinel structure, where the larger Ni^{2+} (r = 0.72 Å) replaces the smaller Co^{3+} at octahedral sites (r = 0.63 Å). XPS spectra, furthermore, also revealed the presence of Ni^{3+} oxidation states that are incorporated into the spinel structure. Note that Ni^{3+} oxidation peaks do not contribute to a feature shift as their atomic radius is very close to that of Co^{3+} (r = 0.62 Å).[78,79]

Evidence of both rock-salt and spinel structures can be observed for compositions between 25% Co and 75% Co. This can be deduced by the presence of both the (200) rock-salt feature at 3.5 nm^{-1} and the (220) spinel feature at 4.8 nm^{-1}. The shift of the (220) rock-salt feature from 6.8 to 6.9 nm^{-1} to higher 1/d in this region is likely due to the limited resolution of electron diffraction, which results in an overlap with the (440) spinel phase feature. The observation of a mixed crystallographic phase is not the result of segregation into spinel cobalt oxide domains and rock-salt nickel oxide domains, as shown by EDX elemental mapping (Fig. S5 in the supplementary material),[62] which reports evidence of a compositionally homogeneous nickel cobalt oxide phase.

D. Electrical conductivity

Another relevant film property, critical for its electrocatalytic performance, is electrical conductivity. As a matter of fact, the electrocatalyst does not only provide active sites for OER but also transports electrons to the electrical circuit via the conductive substrate utilized for the OER studies. Application of the electrocatalysts in AEM electrolyzers therefore requires conductive metallic oxides (>10 S/cm).[6,9,80] Four-point probe measurements of the deposited oxides (Fig. 7) show major differences in film electrical conductivity with an optimal conductivity exhibited from the film with 64 at. % Co, $[(2.4 \pm 0.2) \times 10^2$ S/cm], while the lowest conductivity is observed to be $(4.2 \pm 0.7) \times 10^{-4}$ S/cm for the 7 at. % Co film. All samples with cobalt in the range of 55–70 at. % Co show high conductivities in the order of 2×10^2 S/cm, with a major decrease in conductivity for at. % Co lower than 45 at. % Co and higher than 85 at. % Co. At extremes, the Co_3O_4 outperforms the NiO by almost two orders of magnitude, which is in agreement with literature.[9] It is important to note that the optimal conductivity is found for the at. % Co where the spinel phase is dominant.

Increase in the conductivity from Co_3O_4 to the lowest at. % Co with a pure spinel type structure can be explained by the formation of Ni^{3+} states. These Ni^{3+} states shift the Fermi level upwards toward the occupied valence band maximum and simultaneously form an unoccupied new hole state with Ni 3d character above the Fermi level.[27] This affects the electronic structure of the film through the formation of a half-metallic state, resulting in a considerable increase in the conductivity. In the rock-salt phase, no improvement in conductivity is observed below 25 at. % Co. This can be attributed to the "clean" substitution of homovalent nickel

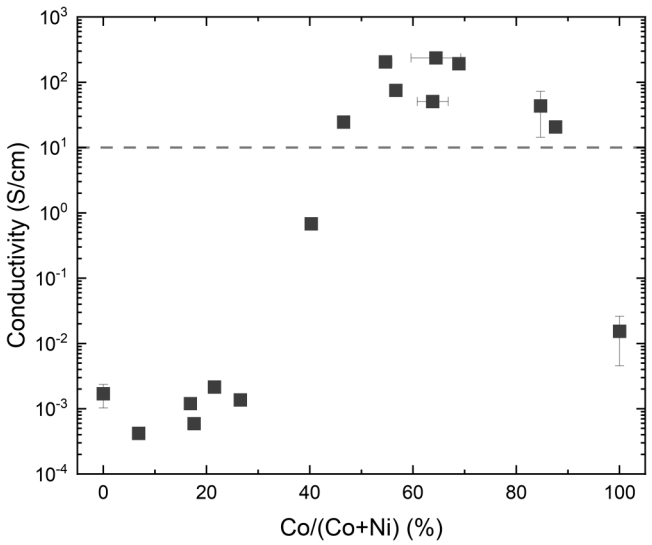

FIG. 7. Four-point probe conductivity measurements of 600 cycle nickel cobalt oxide films (18–30 nm) on 450 nm SiO_2 wafers. Films with conductivities above the 10 S/cm (dashed line) are expected to be suitable for AEM electrolysis based on their electrical performance.

for cobalt, which generates no extra charge carriers.[81] The observed increase in conductivity above 25 at. % Co can be attributed to the increasing amount of Ni^{3+} states and the coexistence of both rock-salt and spinel phases. The Ni^{3+} will enhance the conductivity of the material through generation of extra charge carriers while the presence of the more conductive spinel phase will achieve a similar effect.[79,81]

The mixed oxides, furthermore, show excellent stability in their electrical performance regardless of their composition or electrical performance. After 20 days of storage in ambient conditions, both the 18 at. % Co film and the 69 at. % Co film show no variation in the electrical conductivity. The presence of mixed crystallographic phases in the film also does not affect the film electrical conductivity, as shown by the consistent conductivity of 2×10^1 S/cm for 47 at. % Co films over 140 days of storage.

E. Electrochemical characterization

The OER performance of the cobalt nickel oxide films is evaluated using cyclic voltammetry in 1M KOH solution [Fig. 8(a)]. The electrocatalyst is activated with 100 CV cycles, and the performance is screened through the peak current density, defined as the current density at 1.8 V versus RHE. Evaluation of monometallic oxides shows that Co_3O_4 (36 mA cm^{-2}_{geo}) outperforms NiO (14 mA cm^{-2}_{geo}); an observation that is in accordance with literature.[27,42,82] An optimal peak current density of 59 mA cm^{-2}_{geo} is observed for 80 at. % Co. Films with more than 50 at. % Co outperform Co_3O_4, while lower at. % Co results in decreased peak current densities as compared to Co_3O_4. All mixed oxides are shown to outperform NiO. From these observations, it can be concluded that the spinel phase is more catalytically active as compared to the rock-salt phase and that there is a synergistic effect between cobalt and nickel.

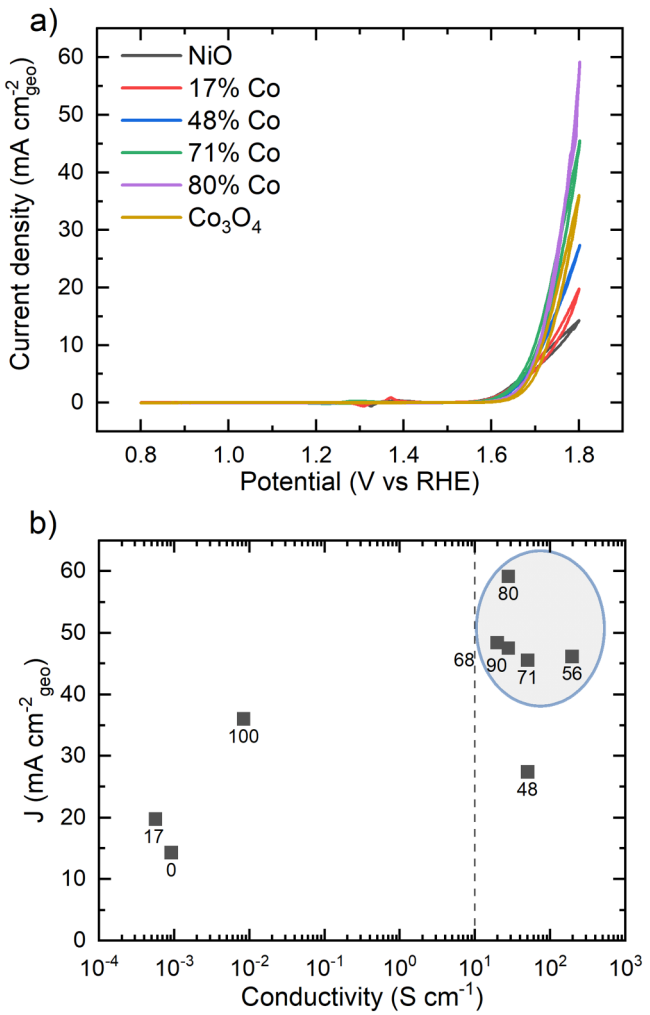

FIG. 8. (a) Cyclic voltammetry measurement of different at. % Co films after 100 cycles. (b) The current density at 1.8 V vs. RHE after 100 cycles as a function of film conductivity. The data labels show the at. % Co before catalysis. The 10 S/cm threshold for conductive metal oxides is indicated by the dashed line, and the most promising electrocatalysts are circled.

The electrocatalytic performance of various at. % Co films shows a similar trend to the electrical conductivity. The relation between the two parameters has been visualized in Fig. 8(b), where the electrochemical peak current density is reported as a function of the electrical conductivity. The at. % Co of the measured films is reported in the datapoint labels. The rock-salt structure electrocatalysts are shown to be both poor conductors and relatively poor electrocatalysts. The spinel-type oxides, on the other hand, show a substantial improvement in the electrocatalyst performance and electrical conductivity upon inclusion of nickel as compared to Co_3O_4. This effect is believed to originate from the formation of

Ni^{3+} states, which not only improve the conductivity but also enhance the absorption of the OH intermediate resulting in better OER performance.[27] Interestingly, there is a variation in the performance for films characterized by both rock-salt and spinel crystallographic phases. The 48 at. % Co shows good electrical conductivity (50 S/cm) but is categorized among the poorest OER electrocatalysts with a peak current density of 27 mA cm_{geo}^{-2}. The 68 at. % Co film, on the other hand, is a slightly poorer conductor (20 S/cm) but shows better OER-catalytic abilities as observed by the peak current density of 48 mA cm_{geo}^{-2}. The improvement in the electrocatalytic performance of the 68 at. % Co film, therefore, suggests that the spinel phase and +3 oxidation states drive the OER, and that besides electrical conductivity, the initial film composition also plays a critical role in the film electrocatalytic performance. The importance of chemical and structural composition of the film can furthermore be understood from the shift in optimal at. % Co for the electrocatalytic performance (80 at. % Co) as compared to the optimum in conductivity (64 at. % Co). This indicates that the electrocatalytic ability does not depend solely on the electrical conductivity but that other material properties, such as crystallographic phase and oxidation states, also affect the performance of cobalt nickel oxide films. Tailoring of electrocatalysts, therefore, relies on the enhancement of the electrical conductivity of the film as well as intrinsic material properties. Crucial material properties of cobalt nickel oxides seem to be the crystallographic phase, where the spinel phase seems to be favorable over the rock-salt phase, and the material oxidation states, where the presence of Ni^{3+} in the film significantly enhances the electrocatalytic performance by lowering the barrier for OER reaction steps. The precise disentanglement of conductivity, composition, and electrocatalytic performance is, therefore, crucial and will be addressed in the future work.

IV. CONCLUSIONS

Plasma-assisted ALD of nickel cobalt oxides with various crystallographic phases has been performed using $CoCp_2$ and Ni $(^{Me}Cp)_2$ as precursors and O_2 plasma as a reactant according to a supercycle process scheme. The ALD process characteristics with self-limiting behavior upon each dosing step have been observed. An increasing GPSC has been observed for more cobalt-rich samples as well as a dependence of individual supercycle growth on material stoichiometry. An ALD process temperature window between 100 and 300 °C has been identified.

The pure rock-salt phase is observed below 25 at. % Co. Within this phase, cobalt and nickel exist primarily in their +2 oxidation state. The absence of higher oxidation states consequently also results in a poor conductivity of 10^{-3} S/cm. Cobalt concentrations exceeding 25 at. % Co result in the formation of more +3 oxidation states and a complementary spinel crystallographic phase, which enhance the material conductivity significantly. An optimal conductivity of $(2.4 \pm 2) \times 10^2$ S/cm is observed for the inverse spinel phase dominated 54 at. % Co film. The films exclusively show the (inverse) spinel structure for cobalt concentrations exceeding 75 at. % Co. Within this $NiCo_2O_4$ inverse spinel structure, a considerable fraction of Ni^{3+} states is observed, which are believed to be the origin of high electrical conductivity. Further increment above 75 at. % Co finally results in spinel structure Co_3O_4.

The electrocatalytic performance is screened through the evaluation of the peak current density and is found to be closely related to the film conductivity. The poorly conducting rock-salt phase films also show limited OER activity. Within the spinel phase, on the other hand, an increase in electrocatalytic performance is observed for films with higher nickel content. This is attributed to Ni^{3+} states, which both enhance the conductivity of the film and the absorption of OH^- during OER. The initial results from this study suggest that the spinel crystallographic phase in combination with abundant Ni^{3+} oxidation states are optimal for OER performance. The complex relation between electrical conductivity and electrocatalytic performance of the cobalt nickel oxide films furthermore suggests that other material properties such the crystallographic phase and oxidation states also significantly impact the electrocatalytic performance. This shows that the ability of ALD to tune material properties provides handles for studying the intrinsic electrocatalytic ability of transition metal oxides. ALD furthermore provides the opportunity to grow extremely thin films (~2 nm) such that the influence of conductivity can be disentangled from the electrocatalytic ability, which will be employed in future work. In general, atomic layer deposition has proven to be a powerful tool for investigation of material composition properties on the electrocatalytic performance.

ACKNOWLEDGMENTS

This work has been carried out within the SCALE Project (No. NWA.1237.18.001) funded jointly by the Netherlands Organization for Scientific Research. The authors would like to thank the co-founders of the project ISPT, Syngaschem, VecoPrecision and Vsparticle and international partners Toyota Motor Europe and FORTH institute. The authors thank E. Langereis (DIFFER) for the illustrations. The authors thank Wim Arnold Bik (Detect99) for performing RBS measurement; Nga Phung for the discussion on the XPS results; Sina Haghverdi Khamene and Ameya Ranade for insights into the OER performance; and Christian A. A. van Helvoirt, Caspar O. van Bommel, Joris J. I. M. Meulendijks, and Janneke J. A. Zeebregts for technical support. M.C. acknowledges the NWO Aspasia program. Solliance and the Dutch province of Noord-Brabant are acknowledged for funding the TEM facility.

AUTHOR DECLARATIONS

Conflict of Interest

The authors have no conflicts to disclose.

Author Contributions

Renee T. M. van Limpt: Formal analysis (lead); Investigation (lead); Validation (lead); Visualization (lead); Writing – original draft (lead); Writing – review & editing (equal). **Marek Lavorenti:** Formal analysis (equal); Investigation (equal); Validation (equal); Writing – review & editing (equal). **Marcel A. Verheijen:** Formal analysis (equal); Investigation (equal); Validation (equal); Writing – review & editing (equal). **Mihalis N. Tsampas:** Conceptualization (equal); Formal analysis (equal); Funding acquisition (equal); Resources (equal); Validation (equal); Writing – review & editing (equal). **Mariadriana Creatore:** Conceptualization (equal); Formal

analysis (equal); Funding acquisition (equal); Resources (equal); Supervision (lead); Validation (equal); Writing – review & editing (equal).

DATA AVAILABILITY

The data that support the findings of this study are openly available in Zenodo at https://doi.org/10.5281/zenodo.7624487, Ref. 83.

REFERENCES

[1]H. Wang, K. H. L. Zhang, J. P. Hofmann, V. A. de la Peña O´Shea, and F. E. Oropeza, J. Mater. Chem. A **9**, 19465 (2021).
[2]N. L. Panwar, S. C. Kaushik, and S. Kothari, Renew. Sustain. Energy Rev. **15**, 1513 (2011).
[3]W. Li, H. Tian, L. Ma, Y. Wang, X. Liu, and X. Gao, Mater. Adv. **3**, 5598 (2022).
[4]International Energy Agency, *Global Hydrogen Review* (OECD, Paris, 2021).
[5]A. Badgett, M. Ruth, and B. Pivovar, *Electrochemical Power Sources: Fundamentals, Systems, and Applications* (Elsevier, Amsterdam, 2022), pp. 327–364.
[6]N. Du, C. Roy, R. Peach, M. Turnbull, S. Thiele, and C. Bock, Chem. Rev. **122**, 11830 (2022).
[7]F. M. Sapountzi, J. M. Gracia, C. J. (Kees-J.) Weststrate, H. O. A. Fredriksson, and J. W. (Hans). Niemantsverdriet, Prog. Energy Combust. Sci. **58**, 1 (2017).
[8]H. A. Miller, K. Bouzek, J. Hnat, S. Loos, C. I. Bernäcker, T. Weißgärber, L. Röntzsch, and J. Meier-Haack, Sustain. Energy Fuels **4**, 2114 (2020).
[9]D. Xu *et al.*, ACS Catal. **9**, 7 (2019).
[10]F. M. Sapountzi, M. Lavorenti, W. Vrijburg, S. Dimitriadou, B. Tyburska-Pueschel, P. Thüne, H. Niemantsverdriet, T. V. Pfeiffer, and M. N. Tsampas, Catalysts **12**, 1343 (2022).
[11]I. Vincent and D. Bessarabov, Renew. Sustain. Energy Rev. **81**, 1690 (2018).
[12]R. R. Raja Sulaiman, W. Y. Wong, and K. S. Loh, Int. J. Energy Res. **46**, 2241 (2022).
[13]P. Shirvanian, A. Loh, S. Sluijter, and X. Li, Electrochem. Commun. **132**, 107140 (2021).
[14]Q. Xu, L. Zhang, J. Zhang, J. Wang, Y. Hu, H. Jiang, and C. Li, EnergyChem **4**, 100087 (2022).
[15]L. Sun, Q. Luo, Z. Dai, and F. Ma, Coord. Chem. Rev. **444**, 214049 (2021).
[16]D. Henkensmeier, M. Najibah, C. Harms, J. Žitka, J. Hnát, and K. Bouzek, J. Electrochem. Energy Convers. Storage **18**, 024001 (2021).
[17]Q. Guo *et al.*, Small **16**, 1907029 (2020).
[18]P. Wang and B. Wang, ACS Appl. Mater. Interfaces **13**, 59593 (2021).
[19]H. Sun, Z. Yan, F. Liu, W. Xu, F. Cheng, and J. Chen, Adv. Mater. **32**, 1806326 (2020).
[20]C. C. L. McCrory, S. Jung, I. M. Ferrer, S. M. Chatman, J. C. Peters, and T. F. Jaramillo, J. Am. Chem. Soc. **137**, 4347 (2015).
[21]L. Zhang, Q. Fan, K. Li, S. Zhang, and X. Ma, Sustain. Energy Fuels **4**, 5417 (2020).
[22]G. Fu *et al.*, Chem. Mater. **31**, 419 (2019).
[23]K. Momma and F. Izumi, J. Appl. Crystallogr. **44**, 1272 (2011).
[24]Z. Hu, L. Hao, F. Quan, and R. Guo, Catal. Sci. Technol. **12**, 436 (2022).
[25]A. Bergmann, E. Martinez-Moreno, D. Teschner, P. Chernev, M. Gliech, J. F. de Araújo, T. Reier, H. Dau, and P. Strasser, Nat. Commun. **6**, 8625 (2015).
[26]R. Zhang *et al.*, ACS Catal. **8**, 3803 (2018).
[27]M. Cui, X. Ding, X. Huang, Z. Shen, T.-L. Lee, F. E. Oropeza, J. P. Hofmann, E. J. M. Hensen, and K. H. L. Zhang, Chem. Mater. **31**, 7618 (2019).
[28]J. Zhao *et al.*, Chem. Eng. J. **435**, 134261 (2022).
[29]M. Harada, F. Kotegawa, and M. Kuwa, ACS Appl. Energy Mater. **5**, 278 (2022).
[30]R. N. Singh, J. P. Pandey, N. K. Singh, B. Lal, P. Chartier, and J.-F. Koenig, Electrochim. Acta **45**, 1911 (2000).
[31]X. Shi, S. L. Bernasek, and A. Selloni, J. Phys. Chem. C **120**, 14892 (2016).
[32]Y. C. Zhang, C. Han, J. Gao, L. Pan, J. Wu, X. D. Zhu, and J. J. Zou, ACS Catal. **11**, 12485 (2021).
[33]Y. Bitla *et al.*, Sci. Rep. **5**, 15201 (2015).
[34]Q. Zhang, Y. Xie, F. Ling, Z. Song, D. Li, Y. Lu, X. Tang, Y. Li, and X. Zhou, Vacuum **196**, 110764 (2022).
[35]X. C. Huang *et al.*, Phys. Rev. B **100**, 115301 (2019).
[36]K. H. L. Zhang, K. Xi, M. G. Blamire, and R. G. Egdell, J. Phys.: Condens. Matter **28**, 383002 (2016).
[37]X. Sun, J. Sun, C. Wu, L. Guo, L. Hou, and C. Yuan, Mater. Today Energy **19**, 100592 (2021).
[38]L. Trotochaud, J. K. Ranney, K. N. Williams, and S. W. Boettcher, J. Am. Chem. Soc. **134**, 17253 (2012).
[39]R. D. L. Smith, M. S. Prévot, R. D. Fagan, S. Trudel, and C. P. Berlinguette, J. Am. Chem. Soc. **135**, 11580 (2013).
[40]A. Ashok, A. Kumar, J. Ponraj, S. A. Mansour, and F. Tarlochan, Int. J. Hydrogen Energy **44**, 16603 (2019).
[41]K. L. Nardi, N. Yang, C. F. Dickens, A. L. Strickler, and S. F. Bent, Adv. Energy Mater. **5**, 1500412 (2015).
[42]X. Deng, S. Öztürk, C. Weidenthaler, and H. Tüysüz, ACS Appl. Mater. Interfaces **9**, 21225 (2017).
[43]V. Viswanathan, K. L. Pickrahn, A. C. Luntz, S. F. Bent, and J. K. Nørskov, Nano Lett. **14**, 5853 (2014).
[44]S. Schlicht, S. Haschke, V. Mikhailovskii, A. Manshina, and J. Bachmann, ChemElectroChem **5**, 1259 (2018).
[45]Y. Cao, Y. Wu, C. Badie, S. Cadot, C. Camp, E. A. Quadrelli, and J. Bachmann, ACS Omega **4**, 8816 (2019).
[46]S. Haschke, D. Pankin, Y. Petrov, S. Bochmann, A. Manshina, and J. Bachmann, ChemSusChem **10**, 3644 (2017).
[47]A. Goulas and J. Ruud van Ommen, J. Mater. Chem. A **1**, 4647 (2013).
[48]H. Van Bui *et al.*, Nanoscale **9**, 10802 (2017).
[49]J. Gascon, J. R. van Ommen, J. A. Moulijn, and F. Kapteijn, Catal. Sci. Technol. **5**, 807 (2015).
[50]R. Zhang, G. van Straaten, V. di Palma, G. Zafeiropoulos, M. C. M. van de Sanden, W. M. M. Kessels, M. N. Tsampas, and M. Creatore, ACS Catal. **11**, 2774 (2021).
[51]J. Rongé, T. Dobbelaere, L. Henderick, M. M. Minjauw, S. P. Sree, J. Dendooven, J. A. Martens, and C. Detavernier, Nanoscale Adv. **1**, 4166 (2019).
[52]K. L. Pickrahn, A. Garg, and S. F. Bent, ACS Catal. **5**, 1609 (2015).
[53]F. Mattelaer, T. Bosserez, J. Rongé, J. A. Martens, J. Dendooven, and C. Detavernier, RSC Adv. **6**, 98337 (2016).
[54]K. L. Pickrahn, Y. Gorlin, L. C. Seitz, A. Garg, D. Nordlund, T. F. Jaramillo, and S. F. Bent, Phys. Chem. Chem. Phys. **17**, 14003 (2015).
[55]Y. Koshtyal, I. Mitrofanov, D. Nazarov, O. Medvedev, A. Kim, I. Ezhov, A. Rumyantsev, A. Popovich, and M. Y. Maximov, Nanomaterials **11**, 907 (2021).
[56]D. J. Hagen, T. S. Tripathi, and M. Karppinen, Dalt. Trans. **46**, 4796 (2017).
[57]S. B. S. Heil, E. Langereis, F. Roozeboom, M. C. M. van de Sanden, and W. M. M. Kessels, J. Electrochem. Soc. **153**, G956 (2006).
[58]M. E. Donders, H. C. M. Knoops, M. C. M. van, W. M. M. Kessels, and P. H. L. Notten, J. Electrochem. Soc. **158**, G92 (2011).
[59]D. Koushik *et al.*, J. Mater. Chem. C **7**, 12532 (2019).
[60]H. L. Lu, G. Scarel, M. Alia, M. Fanciulli, S.-J. Ding, and D. W. Zhang, Appl. Phys. Lett. **92**, 222907 (2008).
[61]C. Gammer, C. Mangler, C. Rentenberger, and H. P. Karnthaler, Scr. Mater. **63**, 312 (2010).
[62]See supplementary material at https://www.scitation.org/doi/suppl/10.1116/6.0002414 for (i) Co-% determination, (ii) ALD process, (iii) EDX measurements of mixed cobalt nickel oxide, (iv) Ni3+-to-Ni2 + ratio, and (v) electrochemical measurements.
[63]See www.detect99.nl for Detect99.

[64]J. A. Maxwell, J. L. Campbell, and W. J. Teesdale, Nucl. Instrum. Methods Phys. Res. Sect. B **43**, 218 (1989).
[65]N. P. Barradas and C. Jeynes, Nucl. Instrum. Methods Phys. Res. Sect. B **266**, 1875 (2008).
[66]J. W. F. Innocent, M. Napari, A. L. Johnson, T. R. Harris-Lee, M. Regue, T. Sajavaara, J. L. MacManus-Driscoll, F. Marken, and F. Alkhalil, Mater. Adv. **2**, 273 (2021).
[67]Y. Koshtyal, D. Nazarov, I. Ezhov, I. Mitrofanov, A. Kim, A. Rymyantsev, O. Lyutakov, A. Popovich, and M. Maximov, Coatings **9**, 301 (2019).
[68]W. M. Haynes, *CRC Handbook of Chemistry and Physics*, 97th ed. (CRC, Boca Raton, 2016).
[69]I. Mitrofanov, D. Nazarov, Y. Koshtyal, I. Ezhov, P. Fedorov, A. Rumyantsev, A. Popovich, and M. Maximov, in *Proceedings 12th International Conference on Nanomaterials - Research & Application (Nanocon)*, Brno, 21–23 Oct. 2020 (Tanger Ltd., Ostrava-Zabreh, 2020), pp. 196–201.
[70]M. C. Biesinger, B. P. Payne, A. P. Grosvenor, L. W. M. Lau, A. R. Gerson, and R. S. C. Smart, Appl. Surf. Sci. **257**, 2717 (2011).
[71]M. C. Biesinger, B. P. Payne, L. W. M. Lau, A. Gerson, and R. S. C. Smart, Surf. Interface Anal. **41**, 324 (2009).
[72]D. Cabrera-German, G. Gomez-Sosa, and A. Herrera-Gomez, Surf. Interface Anal. **48**, 252 (2016).
[73]A. P. Grosvenor, M. C. Biesinger, R. S. C. Smart, and N. S. McIntyre, Surf. Sci. **600**, 1771 (2006).
[74]T.-C. Chang, Y.-T. Lu, C.-H. Lee, J. K. Gupta, L. J. Hardwick, C.-C. Hu, and H.-Y. T. Chen, ACS Omega **6**, 9692 (2021).
[75]P. F. Ndione *et al.*, Adv. Funct. Mater. **24**, 610 (2014).
[76]V. Stevanović, M. d´Avezac, and A. Zunger, J. Am. Chem. Soc. **133**, 11649 (2011).
[77]K. Baraik *et al.*, RSC Adv. **10**, 43497 (2020).
[78]C. F. Windisch, K. F. Ferris, G. J. Exarhos, and S. K. Sharma, Thin Solid Films **420–421**, 89 (2002).
[79]C. F. Windisch, G. J. Exarhos, and R. R. Owings, J. Appl. Phys. **95**, 5435 (2004).
[80]A. Marshall, B. Børresen, G. Hagen, M. Tsypkin, and R. Tunold, Mater. Chem. Phys. **94**, 226 (2005).
[81]T. M. Roffi, K. Uchida, and S. Nozaki, J. Cryst. Growth **414**, 123 (2015).
[82]M. Yu, E. Budiyanto, and H. Tüysüz, Angew. Chemie Int. Ed. **61**, e202103824 (2022).
[83]R. T. M. van Limpt, M. Lavorenti, M. A. Verheijen, M. N. Tsampas, and M. Creatore, (2023). "Control by atomic layer deposition over the chemical composition of nickel cobalt oxide for the oxygen evolution reaction," Zenodo.